

# **Metrology of crystal defects through intensity variations in secondary electrons from the diffraction of primary electrons in a scanning electron microscope**

G. Naresh-Kumar<sup>1\*</sup>, A. Alasamari<sup>1</sup>, G. Kusch<sup>1</sup>, P. R. Edwards<sup>1</sup>, R.W. Martin<sup>1</sup>,  
K. P. Mingard<sup>2</sup> and C. Trager-Cowan<sup>1</sup>

*1. Department of Physics, SUPA, University of Strathclyde, Glasgow G4 0NG, UK*

*2. National Physical Laboratory, Middlesex TW11 0LW, UK*

*\*naresh.gunasekar@strath.ac.uk*

## **ABSTRACT**

Understanding defects and their roles in plastic deformation and device reliability is important for the development of a wide range of novel materials for the next generation of electronic and optoelectronic devices. We introduce the use of gaseous secondary electron detectors in a variable pressure scanning electron microscope for non-destructive imaging of extended defects using electron channelling contrast imaging. We demonstrate that *all scattered electrons*, including the secondary electrons, can provide diffraction contrast as long as the sample is positioned appropriately with respect to the incident electron beam. Extracting diffraction information through monitoring the modulation of the intensity of secondary electrons as a result of diffraction of the incident electron beam, opens up the possibility of performing low energy electron channelling contrast imaging to characterise low atomic weight and ultra-thin film materials. Our methodology can be adopted for large area, nanoscale structural characterisation of a wide range of crystalline materials including metals and semiconductors, and we illustrate this using the examples of aluminium nitride and gallium nitride. The capability of performing electron channelling contrast imaging, using the variable pressure mode, extends the application of this technique to insulators, which usually require conducting coatings on the sample surface for traditional scanning electron microscope based microstructural characterisation.

*Keywords: Electron channelling, secondary electrons, semiconductors and extended defects.*

## 1. INTRODUCTION

Metrology of crystalline defects is crucial for the understanding and development of a wide range of novel materials, as well as for the optimisation of existing and next-generation electronic and optoelectronic devices. Extended defects are often electrically active and usually problematic for electronic devices such as high electron mobility transistors and optoelectronic devices such as AlN-based deep-ultraviolet light emitting diodes [1]. Eliminating or reducing these defects using novel crystal growth techniques becomes paramount, and this leads to a demand for extended defect characterisation tools which are simultaneously rapid to use, non-destructive and capable of investigating large sampling areas while maintaining nanoscale resolution. Electron channelling contrast imaging (ECCI) in the scanning electron microscope [2-4] provides the required capability for studying various materials including metals [5, 6] and semiconductors [7-10]. However, while images of extended defects, similar to those observed in plan-view transmission electron microscopy, can be obtained using ECCI (albeit with lower spatial resolution), the uptake of the technique has not been widespread. The main reasons are (a) the need for additional detectors in specific locations, (b) the limited know-how for achieving the conditions needed for acquiring high quality images, and (c) challenges with characterising low atomic weight, topography-dominated and insulating samples.

This work demonstrates a much wider applicability of ECCI, introducing the use of “standard” secondary electron detectors as well as its suitability for characterising insulating materials and as-grown large area semiconductor wafers. We go on to clarify the advantage of performing ECCI in a gaseous environment. In this case water vapour is used and this plays a dual role in reducing surface charging as well as acting as an amplification medium, thus increasing the signal-to-noise ratio. We also discuss the necessary criteria for performing ECCI in a gaseous environment using non-conventional detectors (for ECCI), namely

gaseous secondary electron detectors [11, 12]. We further demonstrate that diffraction information can also be extracted from monitoring the intensity of secondary electrons by means of Everhart-Thornley detectors, as diffraction of the incident beam leads to a small change in intensity of all backscattered and emitted particles and radiation, including secondary electrons, compared to when no diffraction of the incident beam occurs [4].

We show examples from technologically important semiconductor materials such as GaN, SiC and AlN, with the latter being a low atomic weight and insulating material. While the use of ECCI in the variable pressure scanning electron microscope is particularly useful for characterising wide band gap semiconductors, we stress that the methodology is applicable to all kinds of crystalline samples provided appropriate imaging conditions are used. Figure 1 depicts the present methods used to perform ECCI and the new methodology we introduce to give a much wider applicability of ECCI.

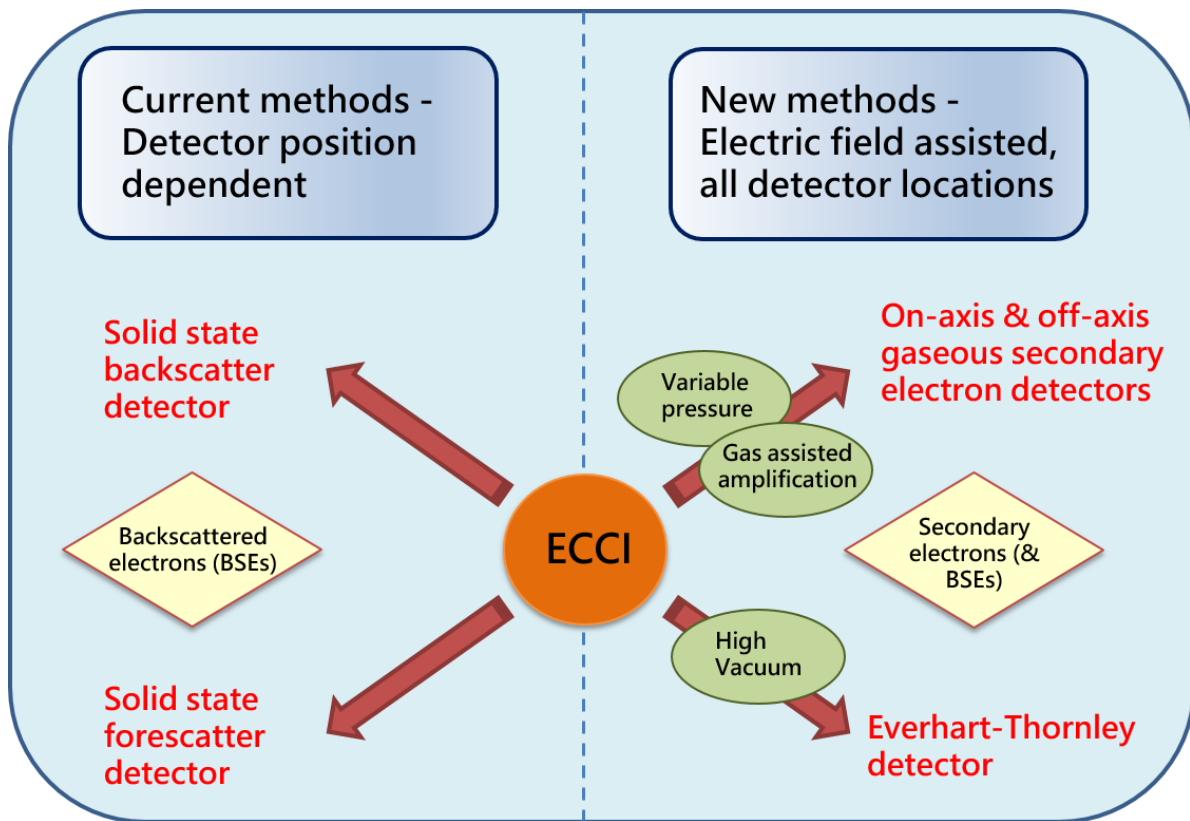


Fig. 1. Schematic depicting the current ECCI acquisition methods (left side) and the proposed new methodologies (right side) allowing a wider application of ECCI for the structural characterisation of materials.

## 2. BACKGROUND AND EXPERIMENTAL METHODS

### 2.1 Electron Channelling Contrast Imaging (ECCI)

Thus far electron channelling contrast images have been obtained by monitoring the intensity of backscattered electrons (see Fig. 1) as the electron beam is scanned over the sample positioned at a Bragg diffraction condition. When the scanning electron microscope is operated at a very high magnification, the angle between the scanned electron beam and the surface remains constant. As a result, for a sample placed at or close to a Bragg angle, any deviation in the crystallographic orientation or in the lattice constant due to local strain is revealed by variation in the contrast in the image. In ECCI it is the small changes in the

intensity of the backscattered electrons which result from changes in diffraction of the incident beam which dominate the contrast in ECCI micrographs.

ECCI micrographs are generally acquired in a field emission scanning electron microscope which provides a low divergence, highly-focused, bright electron probe. Figure 2a shows the various standard commercial detectors which may be used to capture the backscattered electrons and Figs. 2b and 2c reveal dislocations in (0001) GaN and stacking faults in (001) SiC obtained using the solid state forescatter detector and backscattered detector respectively acquired at an electron beam energy of 30 keV. Using ECCI, one can obtain both quantitative and qualitative information on extended defects. For instance in Fig. 2b the threading dislocations are seen as spots with black and white contrast which can be simply counted to estimate the threading dislocation density. Furthermore, monitoring the direction of the black and white contrast for various diffraction conditions allows determination of the types of threading dislocations (screw, edge and mixed) [9]. Similarly, the density of basal plane stacking faults can be estimated from Fig. 2c.

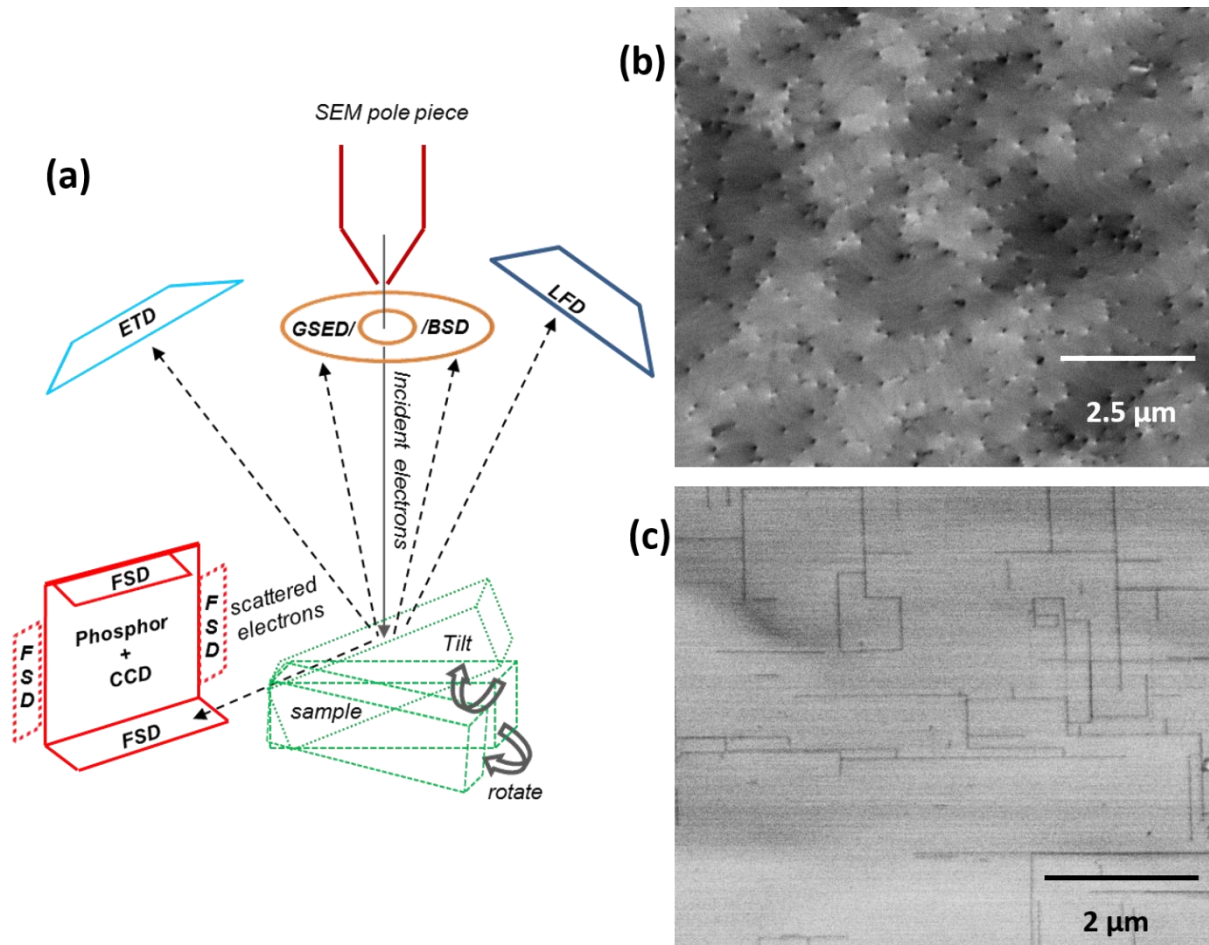


Fig. 2. (a) Schematic of the widely used commercial electron detectors for electron imaging in a variable pressure scanning electron microscope: forescatter detector (FSD), backscatter detector (BSD), on-axis gaseous secondary electron detector (GSED), off-axis GSED otherwise referred to as a large field of view detector (LFD) and Everhart-Thornley detector (ETD) (operable only in high-vacuum mode). (b) ECCI using a FSD, revealing threading dislocations in a (0001) GaN thin film and (c) ECCI using a BSD revealing basal plane stacking faults in a (001) SiC thin film. Both images are acquired using silicon-based solid-state detectors at an electron beam energy of 30 keV. Dislocations are seen as black-white spots and stacking faults are seen as black lines.

## 2.2 Electron scattering inside a variable pressure scanning electron microscope

A comprehensive review of the interactions of the electron beam with materials is reported in Ref. [13]. Here we limit our discussion only to secondary electrons (SEs) and backscattered electrons (BSEs) generated when a focused electron beam interacts with a sample. The secondary electrons can be classified into three types, SE1, SE2 and SE3. The SE1s are the secondary electrons generated directly from interactions of the primary beam with the specimen whereas the SE2s are created by backscattered electrons on their way out from the sample. The SE3s are the electrons scattered from other parts/surfaces inside the scanning electron microscope chamber [13]. We can similarly classify backscattered electrons into three groups: (1) elastically or quasi-elastically scattered electrons which are either scattered coherently or incoherently, through phonon scattering; (2) Inelastically scattered electrons which have lost only a relatively small amount of energy in the order of tens of eV; and (3) inelastically scattered electrons which have lost substantial energy of the order of hundreds of eV. Diffraction effects can be exhibited by all three groups of backscattered electrons as well as secondary electrons [4]. The introduction of gas into the scanning electron microscope chamber leads to additional interactions of the electron beam with gas molecules, as comprehensively reviewed in references [11, 12, 14 and 15]. Here, we broadly classify the incident electron beam in the gaseous environment in two parts: the unscattered beam (retaining the energy distribution and beam size of the incident beam), and the scattered beam where the beam trajectory is broadened [12]. The type of gas used plays a role in the amplification process, and numerous gases including air, H<sub>2</sub>O (water vapour), CO<sub>2</sub>, N<sub>2</sub>O, N<sub>2</sub>, He, NH<sub>3</sub> and CH<sub>3</sub>CH<sub>2</sub>OH have been used to date [16]. Among these gases, water vapour is the most commonly used, and is the one used in our present work. We now consider the detection of scattered electrons using gaseous secondary electron detectors. When the primary electron beam interacts with the material, the secondary

electrons enter the water vapour with a Maxwell-Boltzmann distribution and has a maximum at an energy of  $\approx 3$  eV and range between 0 eV and 50 eV [17]. Those with energy above the first ionization potential of the H<sub>2</sub>O gas ( $\approx 12.7$  eV) can undergo ionizing collisions with H<sub>2</sub>O molecules, producing positive ions and additional electrons known as environmental secondary electrons. These environmental secondary electrons can ionise additional H<sub>2</sub>O molecules (as a cascade process) on their way towards a positively biased collector plate or ring in the gaseous secondary electron detector, which acts as an anode. The current flowing to the anode is detected and used as an amplified secondary electron signal which can be up to three orders of magnitude greater than the signal from the original secondary electrons leaving the sample [18]. The positive bias applied to the collector plate/ring is crucial as it accelerates the environmental secondary electrons, thereby causing additional ionisation events to occur and generating more signal. The positive ions produced during ionisation of the gas in the SEM chamber drift towards the specimen to neutralise the excess surface charge produced on the insulating samples. Electron–gas molecule collisions are also capable of generating photons, negative ions and long lived excited species. Note that the primary electrons and backscattered electrons can also ionise H<sub>2</sub>O molecules along their path, but it is the secondary electrons that have the highest interaction cross section [19] and produce the largest contribution to the signal detected by the gaseous secondary electron detectors [19, 20]. Unlike detectors based on the principle of particle counting, i.e. measuring the number of electrons or ions reaching the anode, gaseous secondary electron detectors monitor the current induced by the flow of charged particles in their vicinity, including both electrons and ions. The magnitude of the current flowing to the anode (amplified signal) depends on the number of charged particles produced during the ionisation process, the drift velocity produced by the applied bias and the distance between the sample and the anode.

A broad review of various types of gaseous detector devices employed in variable pressure scanning electron microscope is given in references [21, 22]. In our present work, we have used two types of gaseous electron detectors, namely an on-axis gaseous secondary electron detector and an off-axis gaseous secondary electron detector referred to as a large field of view detector (see Fig. 2a). The choice and efficiency of the gaseous secondary electron detector devices depend not only on the nature of the specimen and the type of signal being detected but also on the pressure, temperature and the nature of the gas, electrode configuration and the bias. The incident beam profile and the scan speed also play a crucial role in determining the amount of information that can be extracted from the gaseous secondary electron detectors.

### **3. RESULTS AND DISCUSSION**

#### **3.1 ECCI obtained using gaseous secondary electron detectors**

Contrast in electron micrographs arise from variations in the intensity of various signals as the beam is rastered across the sample, providing information on properties such as composition, surface topography and crystal orientation. Compositional information can be obtained using backscattered electrons, whereas low-energy surface-sensitive secondary electrons are usually used to provide topographic information. However, as discussed previously, if the crystal is oriented for Bragg diffraction of the incident beam (“*channelling in*” condition), contrast due to diffraction effects can also be obtained from any emitted signal [4]. Since gaseous secondary electron detectors collect all types of electrons produced by the ionised gas, they can produce images with both diffraction and topographic contrast. This is the new approach for ECCI illustrated in the top-right part of Fig. 1. To demonstrate this, Fig. 3a shows an ECCI micrograph acquired at an electron beam energy of 30 keV, from an AlN thin film using a large field detector revealing surface steps (similar to those observed using

atomic force microscopy) and threading dislocations due to diffraction effects. Figure 3b shows the ECCI micrograph simultaneously acquired from the same area using a conventional solid-state forescatter detector. There is no major difference seen in the dislocation contrast from the ECCI micrographs acquired using the large field detector and forescatter detectors, although the latter collects only the high energy backscattered electrons whereas the former collects both secondary electrons and backscattered electrons. However, careful inspection reveals minor differences between the images. Surface steps are not so clear in Fig. 3b, since the forescatter detector is not in an optimised position and it does not detect secondary electrons which enhance the topographic contrast [23]. The ECCI in Fig. 3a and 3b was acquired by tilting the sample to  $64.6^\circ$  from the surface normal (for the forescatter detector geometry) with a working distance of  $\approx 11$  mm and a gas pressure of 0.6 mbar. The large field detector bias was set to  $\approx +230$  V and a 100  $\mu$ s dwell time was used with an image resolution of  $2048 \times 1768$  pixels. This combination of imaging parameters was chosen in order to optimise the ECCI micrographs; the impact of varying detector bias, gas pressure, working distance and scan rate on the dislocation contrast and the image quality is presented in the supplementary information (Figs. S1 – S4). We have applied fast Fourier transform band-pass filtering to remove horizontal lines produced due to gas fluctuation during the scanning (see supplementary Fig. S4). Since the AlN thin film is a single crystal, it was also possible to acquire an electron channelling pattern (ECP) using the large field detector to acquire an image at low magnification, as shown in Fig. 3c. At low magnification, as the beam is scanned over the sample, it changes its angle with respect to the surface of the sample. This results in different planes of the crystal satisfying the Bragg condition, giving rise to the appearance of overlapping Kikuchi bands superimposed on an image of the sample, i.e., the ECP. The solid yellow circle shows the pattern centre corresponding to the optical axis of the scanning electron microscope, which allows determination of the

diffraction conditions ( $\mathbf{g}$  vector) for classifying various extended defects [9]. The image in Fig. 3d shows the electron backscatter diffraction pattern (EBSD) pattern acquired using the same camera/detector position as the ECCI micrograph shown in Fig. 3b. The yellow cross reveals the pattern centre estimated by the commercial software (Oxford Instruments) for electron backscatter diffraction analysis. The pattern centre of an EBSD pattern indicates the relative position of the EBSD pattern with reference to the incident electron beam position on the sample. Note that the ECP and EBSD pattern are both generated as a result of diffraction effects, where the former is due to the incoming beam diffraction and the latter is due to the outgoing beam diffraction [24]. Note that the collection angle for an ECP from our SEM is  $\approx 10^\circ$ , which is much smaller than for the EBSD pattern shown in Fig 3d where the pattern width is  $\approx 62^\circ$  (and  $\approx 49^\circ$ ) along the X and Y directions, respectively. The EBSD and the ECP pattern centres occur at equivalent points on the EBSD and ECP patterns. There is a  $180^\circ$  inversion of the EBSD pattern with respect to the ECP; this is due to the EBSD detector coordinates selected in the software used to acquire the EBSD pattern.

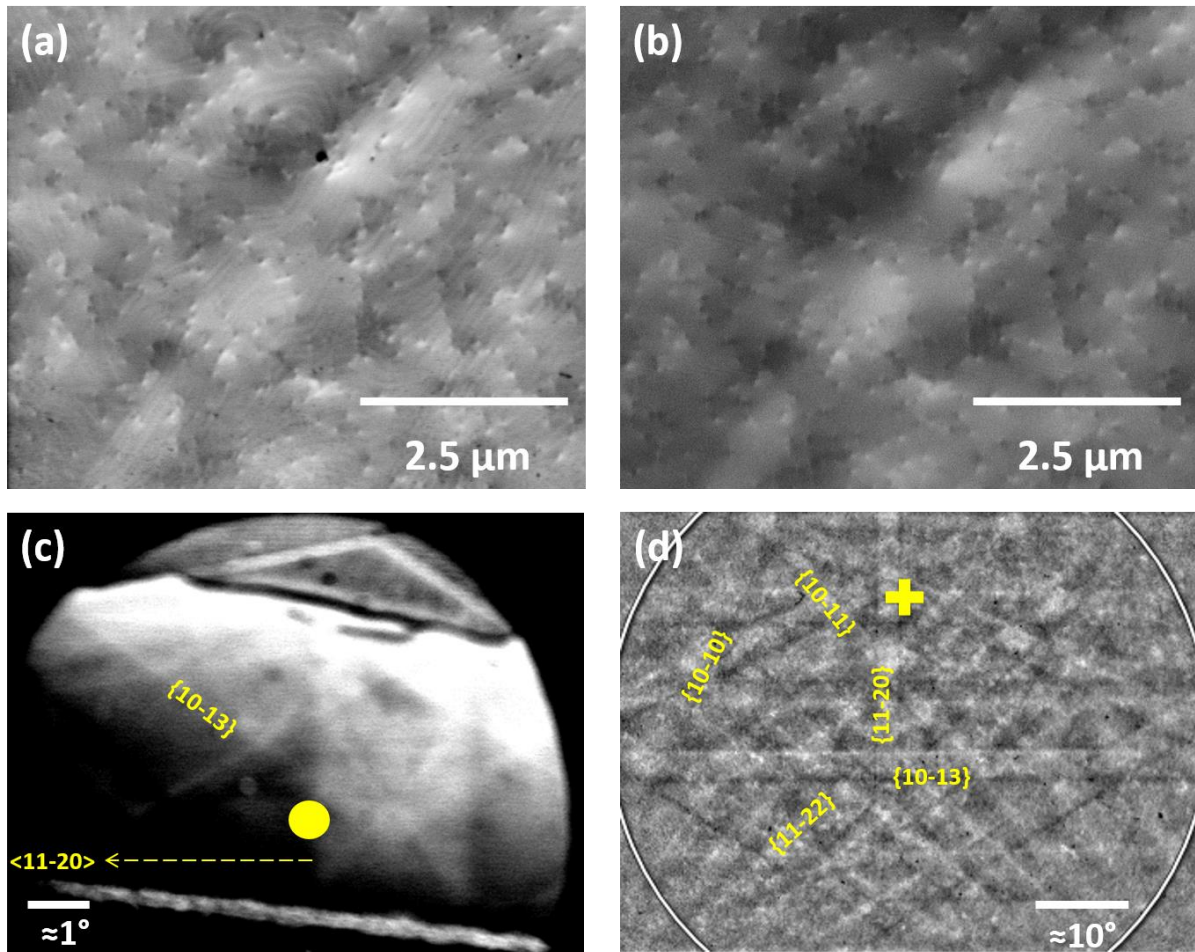


Fig. 3. (a) ECCI of an AlN thin film acquired at  $64.6^\circ$  sample tilt and a beam energy of 30 keV using the large field detector, (b) simultaneously acquired ECCI using conventional forescatter detectors underneath the electron backscatter diffraction detector, (c) electron channelling pattern corresponding to the ECCI micrographs, the solid yellow circle is the pattern centre and identifies the diffraction condition of  $\langle 11-20 \rangle$  marked by dotted yellow arrow at which the ECCI micrograph was acquired, (d) electron backscatter diffraction pattern revealing the estimated pattern centre (yellow cross), a number of the bands are labelled with the planes from which diffraction occurred. For this sample, the total threading dislocation density estimated from the ECCI is  $(1.2 \pm 0.3) \times 10^9 \text{ cm}^{-2}$ .

Among the methods for performing ECCI together with EBSD [25-27], the most common approach is to use the solid state backscattered electron detector mounted or placed under the pole piece to acquire an ECCI micrograph and then tilt the sample to  $\approx 70^\circ$  to perform EBSD [25]. Our present approach of performing ECCI by using gaseous secondary electron detectors, allows the sample to be tilted for the backscattered as well as foreshattered ECCI geometry to image dislocations and still determine the diffraction conditions from ECPs without utilising the EBSD detector. This removes the necessity for using a backscatter detector under the pole piece and also provides an unrestricted movement of the EBSD detector for a subsequent quantitative microstructural analysis. We determine the diffraction condition from ECPs where possible because of their greater angular resolution. Figs. 3 (c) and (d) indicate that incident electron beam was diffracted from one of the  $\{11-20\}$  planes; hence a  $\mathbf{g}$ -vector of  $\langle 11-20 \rangle$  was selected [9]. Due to the electric field between the sample and the gaseous secondary electron detector (as a result of the applied bias), the directionality of the electrons coming out from the sample and the position of the detector do not play a crucial role: the secondary electrons can still carry the diffraction information since the crystal is at, or close to, a Bragg diffraction condition for the incident electron beam. This is demonstrated in Fig. 4, which shows ECCI micrographs acquired at a gas pressure of 1 mbar using an on-axis gaseous secondary electron detector with the sample in the backscattered electron geometry (Fig. 4a) and in the foreshatter geometry (Fig. 4b), both at an electron beam energy of 30 keV. We have also demonstrated the diffraction contrast from secondary electrons using the large field of view detector (see Fig. S5 in supplementary information). Although the gaseous secondary electron detectors are in a fixed position, they are capable of acquiring ECCI micrographs in both the scattering geometries as demonstrated in Fig. 4. Figure 4a also shows clusters of dislocations (e.g. within the yellow circle) where individual dislocations of  $\approx 30$  nm apart can still be resolved even at a gas pressure of 1 mbar. A

pressure limiting aperture on the on-axis gaseous secondary electron detector helps to minimise the beam skirt at higher gas pressures. Since the anode is directly above the sample surface and concentric with the primary electron beam, the subsequent electric field is nearly constant between the sample and the detector [28]. Here, the flow of electrons to the anode is equivalent to the flow of ions to the grounded specimen stub. Hence identical signal currents can be acquired either from the anode or at the grounded sample stub/stage [28]. This is not the case in off-axis gaseous secondary electron detectors where the electric field is not linear and can have an effect on the ionisation efficiency [28]. We did not notice any appreciable difference in the image quality between the images acquired using on-axis and off-axis gaseous secondary electron detectors. The experimental settings and the type of sample (see supplementary information Fig. S6) determine the detector choice. For materials with extended defects threading towards the sample surface, the contrast seen in the ECCI micrograph is mainly due to surface relaxation effects [4], hence all the threading dislocations may be seen in most diffraction conditions (multi-beam conditions) and in any sample geometry (see supplementary information Fig. S5). However, appropriate diffraction conditions are necessary to increase the spatial resolution as well as the ECCI signal intensity. Our present approach to performing ECCI opens up new prospects for simultaneous use of other scanning electron microscope based techniques such as cathodoluminescence and X-ray spectroscopy.

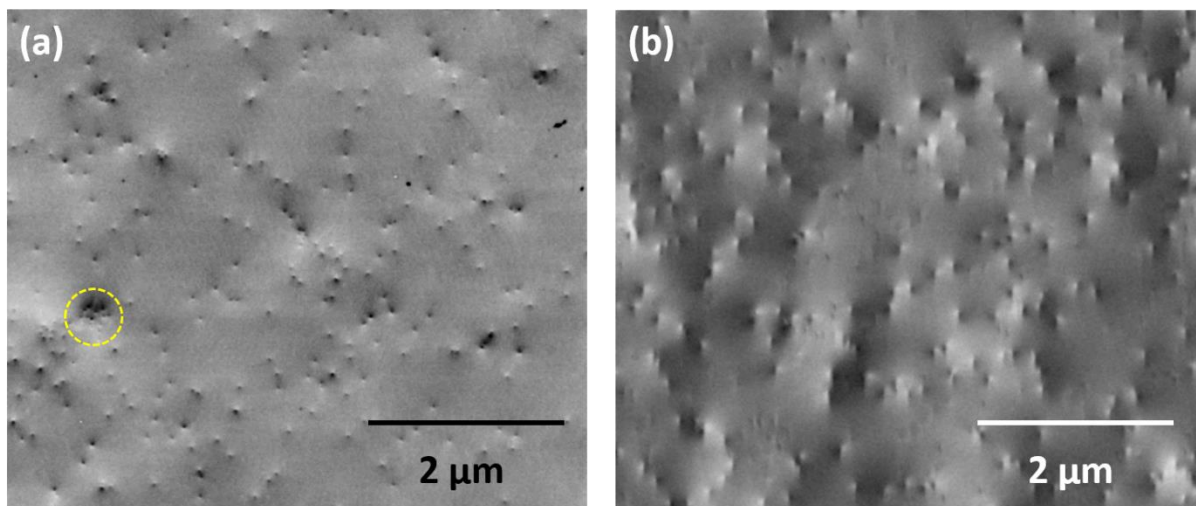


Fig. 4. ECCI micrographs of an AlN thin film measured using an on-axis gaseous secondary electron detector: (a) image acquired with a sample tilt of  $0^\circ$  and (b) with  $65^\circ$  tilt with electron beam energy of 30 keV. Note the images are not from the same area of the sample. The yellow circle highlights a cluster of dislocations in which the individual dislocations  $\approx 30$  nm apart can still be resolved with a gas pressure of 1 mbar.

### 3.2. Effect of incident beam diffraction demonstrated using Everhart-Thornley detector

The influence of incident beam diffraction (*channelling in*) on the energy and momentum distribution of the backscattered electrons has been discussed previously [29]. The diffraction of the incident electron beam has a significant impact on the subsequent coherent and incoherent electron scattering. Having demonstrated the effect of *channelling in* at low vacuum using gaseous secondary electron detectors, here we make evident the effect of *channelling in* at high vacuum using conventional secondary electron detectors. This is the second new approach for ECCI illustrated in the lower-right part of Fig. 1. We demonstrate it in Fig. 5, which shows ECCI acquired at 30 keV and 4 nA from a GaN epilayer revealing threading dislocations and sub-grains. This was acquired at high vacuum ( $10^{-6}$  mbar) using an Everhart-Thornley detector and a foreshorter detector positioned below the electron backscatter diffraction detector. The image shown in Figure 5a is acquired using an Everhart-

Thornley detector biased to +250 V, to attract all of the secondary electrons. Figure 5b is acquired using the same Everhart-Thornley detector with a detector bias of -150 V, to repel secondary electrons and collect backscattered electrons. Normally, images formed with secondary electrons do not show significant orientation contrast as in general samples will not be placed to result in diffraction of the incident electron beam. However, as long as the sample is oriented towards the incident beam close to a Bragg diffraction condition (*channelling in* condition), ECCI can also be obtained using secondary electrons as shown in Fig. 5a. Since the Everhart-Thornley detector is not in an optimised location to capture backscattered electrons for the chosen sample tilt, the image in Fig 5b has a lower signal-to-noise as compared to the image in Fig 5a. Although the contrast for individual threading dislocations is poor, the sub-grains are still revealed. The ECCI micrograph displayed in Fig. 5c is acquired with the forescatter detector close to the sample and in a condition where topographic contrast can be enhanced; as a result surface steps can be clearly seen, in addition to dislocations. On the other hand the ECCI micrograph in Fig. 5d is acquired under conditions optimised to reduce topographic effects [23] while still maintaining the diffraction contrast, and hence the surface steps are not seen as clearly as in Fig. 5c.

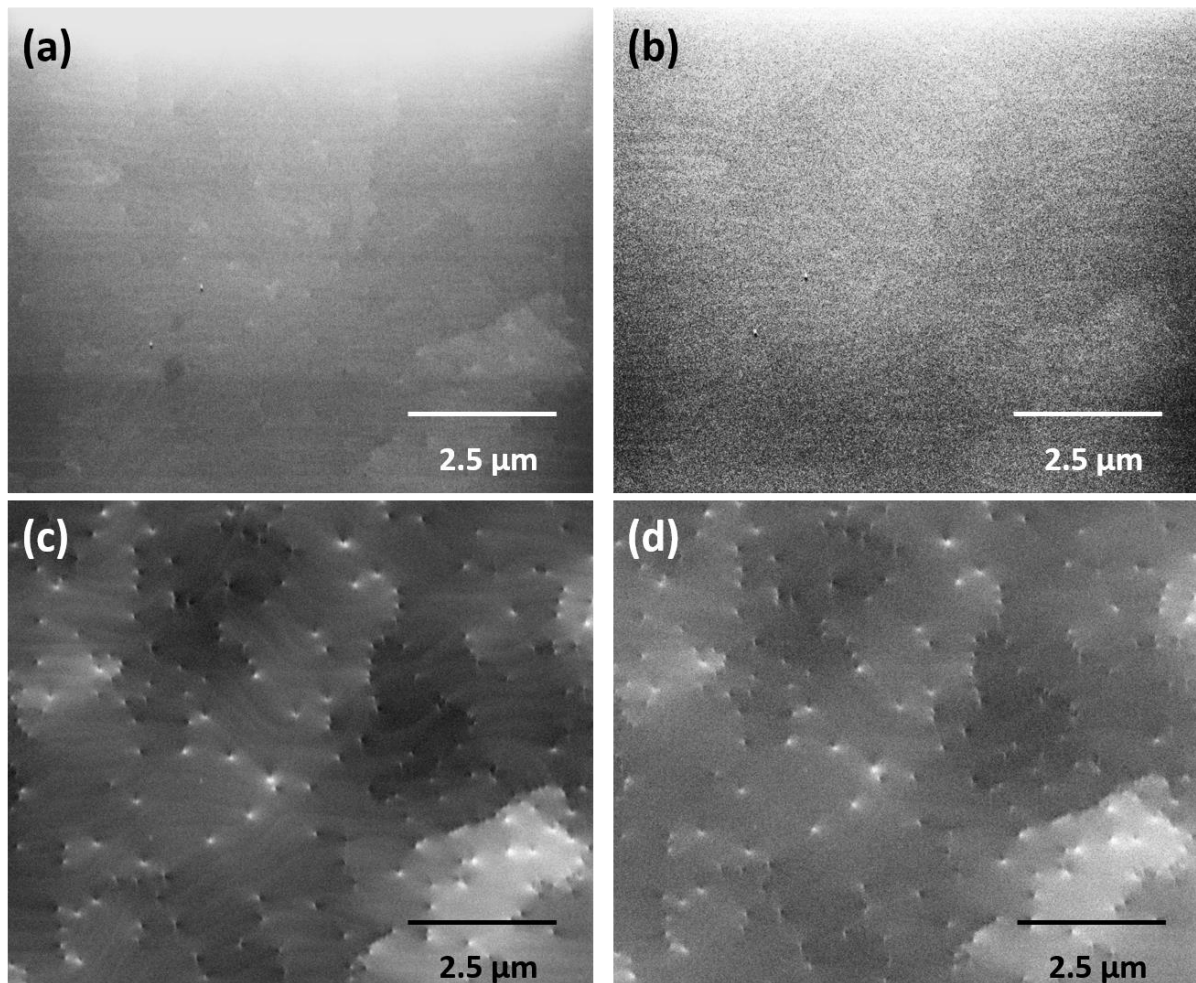


Fig. 5. (a) ECCI acquired at 30 keV from a Si-doped GaN thin film using an Everhart-Thornley detector at a +250 V bias to collect predominately all the secondary electrons as well as some backscattered electrons, (b) ECCI acquired using an Everhart-Thornley detector at -150 V to collect backscattered electrons, still revealing the sub-grain contrast and topography with reduced signal-to-noise, and (c) ECCI acquired using an forescatter detector closer to the sample and d) slightly farther away from the sample. All the images were acquired with the same beam current.

### 3.3. Low voltage ECCI

Low voltage SEM has the advantage of producing high surface sensitivity images due to the smaller penetration depth of the primary electrons. This limits the secondary electron

emission to a shallow surface region with high secondary electron yield [30]. However, the lower probe currents available at low voltages and the chromatic aberration due to the beam spread from the electron source, can affect the image contrast. Novel electron optics, exploiting beam deceleration techniques [30], can help in obtaining ECCI micrographs below 5 keV. This is shown in Figure 6 where we have compared ECCI micrographs acquired at an electron beam energy of 2 keV obtained using the Everhart-Thornley detector with an in-lens secondary electron detector. The latter predominately collects the SE1s [31].

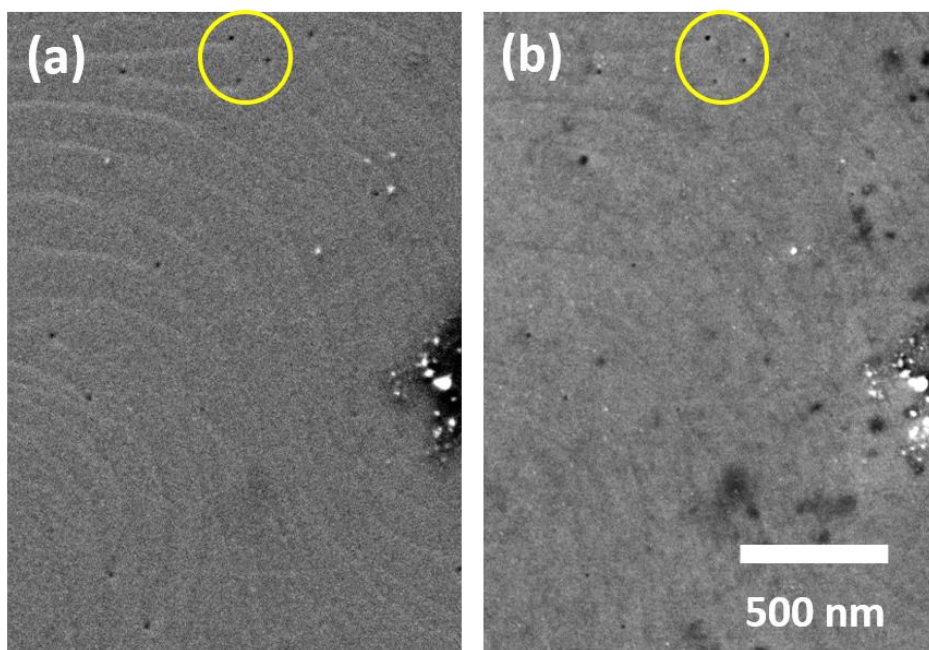


Fig. 6. ECCI from a Si-doped GaN acquired at 2 keV, without any sample tilt and with the same beam current using an (a) Everhart-Thornley detector and (b) in-lens secondary electron detector. The yellow circles highlight selected dislocations.

We have also performed ECCI in high vacuum at a higher incident beam energy (20 keV) in the Zeiss SEM to understand the difference between the image contrast from an in-lens secondary electron detector and an Everhart-Thornley detector. We have also compared the obtained results with the pole-piece mounted backscatter detector. This is shown in Fig. 7. We first optimised the diffraction condition using the pole-piece mounted backscatter

detector and following this, we have acquired the secondary electron images. The ECCI micrographs obtained using the backscatter detector and the Everhart-Thornley detector look similar since the former collects only BSE and the latter collects predominantly the SE2 and BSE [30]. However clear differences are observed in the ECCI micrographs obtained using the Everhart-Thornley detector and the in-lens detector. It appears to be that the retarding electrostatic field of the Zeiss Gemini column acts as a low-pass energy filter for secondary electrons, allowing predominantly SE1 electrons into the SEM column and filtering out most other secondary electrons [31, 32]. The same electrostatic field can also act as a high-pass energy filter enabling collection of predominantly SE2s by the Everhart-Thorley detector [32]. This could explain the observed differences seen in Figures 7b and 7c. The position of the in-lens secondary electron detector determines the number of backscatter electrons reaching it; this depends on the electron-optics design which varies between different SEM manufacturers [31]. Although the in-lens secondary electron detector can detect a fraction of the backscattered electrons, they have very little influence on the acquired images using the in-lens secondary electron detector [31]. It is worth noting that the black white contrast direction for the dislocations in all the three images is similar (see yellow circles in Fig. 7) but the magnitude of the strain profile is different (see Figs. 7b and 7c).

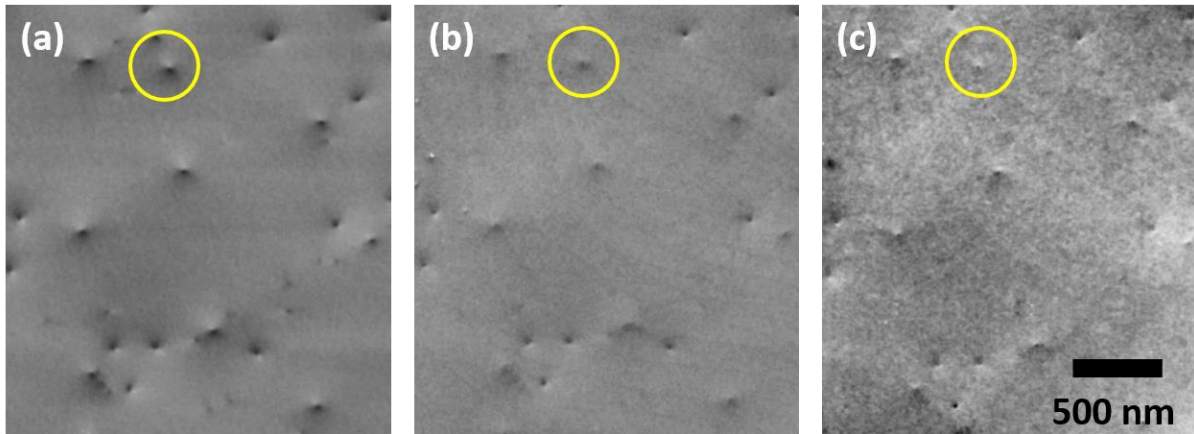


Fig. 7. (a) ECCI from a Si-doped GaN acquired at 20 keV without any sample tilt and with the same beam current and not moving the sample using the BSD, (b) ETD and (c) in-lens SE detector. Dislocation contrast can be seen in the SE2 dominated image (b) as well as in the SE1 dominated image (c). The dislocation contrast looks similar to the images produced due to the backscattered electrons. While the in-lens SE detector tends to emphasise surface contamination, careful inspection shows that the same dislocations are visible with similar contrast black-white contrast as highlighted by yellow circles.

#### 4. CONCLUSION

In summary, we have demonstrated an innovative approach to analysing extended defects using gaseous secondary electron detectors to perform ECCI in a variable pressure scanning electron microscope. The contrast in our ECCI micrographs is a result of changes in the diffraction of the incident electron beam. It is this diffraction of these incoming electrons, for a sample placed in a suitable geometry, that produces diffraction contrast (albeit small) in the secondary electron signals detected in the scanning electron microscope. The position of the gaseous secondary electron detectors is not crucial for performing ECCI, unlike presently available solid-state detectors. Extracting diffraction information through secondary electrons opens up the possibility of performing low energy ECCI for improving the spatial resolution

of this technique. This new approach to performing ECCI also opens up more opportunities for simultaneous use of other scanning electron microscope based techniques for analysing a wide range of crystalline materials.

## **APPENDIX A: DESCRIPTION OF SAMPLES AND IMAGE ACQUISITION**

### **CONDITIONS**

The 1600 nm thick n-type GaN (Fig. 2b) was grown by metalorganic vapour phase epitaxy (MOVPE) using a Thomas Swan showerhead reactor. A 30 nm GaN nucleation layer was first grown at 525 °C on a sapphire substrate. This nucleation layer was then annealed briefly at a GaN growth temperature of 1023 °C prior to thin film growth [33]. The 8 µm thick 3C-SiC was grown by chemical vapour deposition on Si (001) (Fig. 2c) [34]. The 5 µm thick AlN sample was grown by hydride vapour phase epitaxy and was purchased from Kyma Technologies, USA (Figs. 3 and 4). The 3 µm thick unintentionally doped GaN was grown on top of GaN nanocolumns by a nano-pendeo-epitaxy process using a Thomas Swan showerhead MOVPE reactor (Figs. 5, 6 and 7). The underlying nanocolumns were fabricated on GaN/sapphire templates using a lithography process [35].

ECCI micrographs shown in Figs. 2 to 5 were acquired using the FEI (now Thermo Fisher) Quanta 250 FEG-SEM. Typically, electron beam energy of 30 keV, beam currents between  $\approx 2 - 4$  nA, working distances between 10 – 16 mm and gas pressures between 0.5 – 1 mbar were used to perform ECCI in a low vacuum mode. ECCI micrographs shown in Figs. 6 and 7 were acquired using the Zeiss Auriga 60 with the Gemini column in high vacuum at 2 keV and 20 keV respectively. In order to achieve an acceptable signal to noise, the ECCI micrographs obtained using the gaseous secondary electron detector was acquired with a resolution of  $2048 \times 1768$  pixels with a 100 µs dwell time and a detector bias set between +230 V to +250 V. An Oxford instruments forescatter detector was used to acquire the

images shown in Figs. 2b, 3b, 5c, 5d and an Oxford Instruments Nordlys electron backscatter diffraction camera was used to acquire the electron backscatter diffraction pattern shown in Fig. 3d. An FEI quadrant backscattered electron detector was used to collect the image shown in Fig. 2c whereas Figs. 3a, 3c, and Fig. 4 were captured using the off-axis large field of view detector and on-axis gaseous secondary electron detector respectively. We used an Everhart-Thornley detector to acquire the ECCI micrographs displayed in Figs. 5a and 5b.

## **APPENDIX B: ON AND OFF-AXIS GASEOUS SECONDARY ELECTRON DETECTORS**

The on-axis gaseous secondary electron detector is a metallic ring generally mounted under the pole piece of the scanning electron microscope, i.e. concentrically around the optical axis of the microscope. The metallic ring is generally made of gold and is biased (usually with a voltage,  $V_{GSED} = +30 \text{ V}$  to  $+250 \text{ V}$ ) to attract low energy electrons. The bottom of the metallic ring has a pressure limiting aperture (PLA), the one used in our present work was  $500 \mu\text{m}$  in diameter. This helps to separate the high pressure region (sample chamber) and the low pressure region (electron optics column) in the scanning electron microscope. The PLA also helps in reducing the skirt effect especially at higher chamber pressures, but reduces the field of view to only  $500 \mu\text{m}$ . However a PLA with  $1000 \mu\text{m}$  in diameter is also commercially available to increase the field of view. The off-axis gaseous secondary electron detector is a curved metallic plate placed off-axis from the scanning electron microscope column allowing a larger field of view with a maximum pressure limit of  $1.5 \text{ mbar}$ . In our scanning electron microscope both the detectors use the same external amplifier and the associated electronics, such that only one can be used at a time. Due to the different position of the detectors with respect to the sample, the electric fields around the anodes can be different.

## **APPENDIX C: ASSESSMENT OF EXTENDED DEFECT DENSITIES**

ECCI can yield information from larger field of view images, where statistically significant numbers for defect densities can be estimated. However, care has to be taken in estimating the threading dislocation density as different samples exhibit different defect distributions, ranging from completely random to clustered behaviour. It is also possible to have different distributions of threading dislocation from different areas within a single sample grown on large substrates. The threading dislocations and basal plane stacking faults were estimated solely from plan view images with an area of  $\approx 40 \mu\text{m}^2$ . We use a minimum of three ECCI micrographs from different scan areas where individual dislocations can be resolved to estimate the total threading dislocations density.

### **Author contributions**

G.N.K. conceived and designed the study and carried out the main experiments and wrote the paper. A. A., G. K. and K.P.M. performed experiments for the supplementary information and helped in analysing the data. P.R.E, R.W.M and C.T.C helped in analysing the data, discussed the results, and helped in writing the manuscript. All the authors read and commented on the manuscript.

### **Declaration of competing interest**

The authors declare no competing financial interests.

## **ACKNOWLEDGEMENTS**

We would like to thank all our crystal growth colleagues for providing samples for our ECCI studies. Thanks to Prof. Peter Parbrook, University College Cork, Ireland, Dr Nagarajan Subramanian, Aalto University, Finland, Dr Tim Wernicke, TU Berlin, Germany and Dr Philip Shields and Dr Chaowang Liu, University of Bath, UK for providing a range of III-nitrides samples. Special thanks to Dr Aimo Winkelmann for his critical comments on the

manuscript. This work was supported by the EPSRC project EP/M015181/1, “Manufacturing nano- GaN” and EP/P015719/1, “Quantitative non-destructive nanoscale characterisation of advanced materials”. The data that support the findings of this study can be found online under DOI .....

### **Supplementary information**

Supplementary information accompanies this paper. The data that support the findings of this study can be found online under DOI ....., Alternatively, it is also available from the corresponding author on request.

### **REFERENCES:**

1. Y. Taniyasu, M.Kasu and T. Makimoto, *Nature*, **18** (2006) 325.
2. H. Kriaa, A. Guitton and N. Maloufi *Scientific Reports* **7** (2017) 9742.
3. P. G. Callahan, B. B. Haidet, D. Jung, G. G. E. Seward, and K. Mukherjee *Phys. Rev. Materials* **2** (2018) 081601(R).
4. D. C. Joy “Electron Channeling Patterns” in *SEM microcharacterization of semiconductors*”, eds. D. B. Holt and D. C. Joy, Academic Press, London 1989.
5. S. Zaefferer and N.-N. Elhami, *Acta Mater.* **75** (2014) 20.
6. B.E. Dunlap et al, *Ultramicroscopy* **184** (2018) 125.
7. R. J. Kamaladasa, W. Jiang, Y. Picard *Journal of Elec. Mat.*, **40** (2011) 11.
8. A. Schulze et al *Nanoscale*, **10** (2018) 7058.
9. G. Naresh-Kumar et al, *Phys. Rev. Lett.*, **108** (2012) 135503.
10. J. I. Deitz et al, *Appl Phys Lett.*, **109** (2016) 062101.
11. G.D. Danilatos, *Journal of Microscopy*, **160** (1990) 9.
12. A. M. Donald, *Nature Materials* **2** (2003) 511.

13. J. I. Goldstein et al., *Scanning Electron Microscopy and X-ray microanalysis*, Plenum press, New York (1981).
14. D. J. Stokes, *Phil. Trans. R. Soc. Lond. A* **361** (2003) 2771.
15. S. W. Morgan and M. R. Phillips *J. Appl. Phys.* **100** (2006) 074910.
16. T. W. Shanley, F. Bonnie, J. Scott and M. Toth *Appl. Mater. Interfaces* **8** (2016) 27305.
17. L. Reimer, *Scanning electron microscopy*, Springer New York (1985)
18. B. L. Thiel et al *Journal of Microscopy*, **187** (1997) 143.
19. A. Mohan, N. Khanna, J. Hwu, and D. C. Joy, *Scanning* **20** (1998) 436.
20. B. L. Thiel, M. Toth, R. P. M. Schroeemges, J. J. Scholtz, G. van Veen, and W. R. Knowles, *Rev. Sci. Instrum.* **77** (2006) 033705.
21. A. L. Fletcher et al *J. Phys. D: Appl. Phys.* **30** (1997) 2249.
22. G.D. Danilatos, *Journal of Microscopy*, **245** (2012) 171.
23. O.C. Wells, *Scanning*, **2** (1979) 199.
24. A. Winkelmann, C. Trager-Cowan, F. Sweeney, A. P. Day and P. Parbrook, *Ultramicroscopy* **107** (2007) 414.
25. I. Gutierrez-Urrutia, S. Zaefferer and D. Raabe *Scripta Materialia*, **61**, 737 (2009).
26. C. Trager-Cowan, F. Sweeney, P.W. Trimby, A. P. Day, A. Gholinia, N.-H. Schmidt, P. J. Parbrook, A. J. Wilkinson and I. M. Watson, *Phys. Rev. B* **75** (2007) 085301.
27. H. Mansour et al, *Scripta Materialia* **84** (2014) 11.
28. B. L. Thiel *Microchim Acta* **155** (2006) 39.
29. A. Winkelmann et al, *Journal of Microscopy*, **00** (2017) 1.
30. J.R. Michael, D. C. Joy and B. J. Griffin *Microsc Microanal* **15** (2009) 660.
31. B. J. Griffin *Scanning*, **33** (2011) 162.
32. K. Kumagi and T. Sekiguchi *Ultramicroscopy*, **109** (2009) 368.

33. D. A. Wood, P. J. Parbrook, P. A. Lynch, M. Lada, and A. G. Cullis, *Phys. Status Solidi A* **188** (2001) 641.
34. L. Y. Lee, M. Frentrup, P. Vacek, M. J. Kappers, D. J. Wallis and R. A. Oliver J. *Appl. Phys.* **125** (2019) 105303.
35. C. N. Huang, P. A. Shields, D. W.E. Allsopp and A. Trampert *Philosophical Magazine*, **93** (2013) 3154.

## Supplementary information

### **Metrology of crystal defects through intensity variations in secondary electrons from the diffraction of primary electrons in a scanning electron microscope**

G. Naresh-Kumar<sup>1\*</sup>, A. Alasamari<sup>1</sup>, G. Kusch<sup>1</sup>, P. R. Edwards<sup>1</sup>, R.W. Martin<sup>1</sup>,  
K. P. Mingard<sup>2</sup> and C. Trager-Cowan<sup>1</sup>

*1. Department of Physics, SUPA, University of Strathclyde, Glasgow G4 0NG, UK*

*2. National Physical Laboratory, Middlesex TW11 0LW, UK*

[\\*naresh.gunasekar@strath.ac.uk](mailto:*naresh.gunasekar@strath.ac.uk)

#### **S1 Effect of detector bias**

The metallic ring/plate of the gaseous secondary electron detectors (GSEDs) are biased with a voltage, typically up to +250 V, to attract low energy electrons. The environmental secondary electrons are accelerated by this detector bias which helps to further ionize the water vapour on their way to the detector, producing an amplified electron current which can be up to three orders of magnitude greater than the original secondary electron current leaving the sample [1]. Changing the detector bias has a significant influence on the signal to noise ratio of the acquired images; this is shown in Fig. S1.

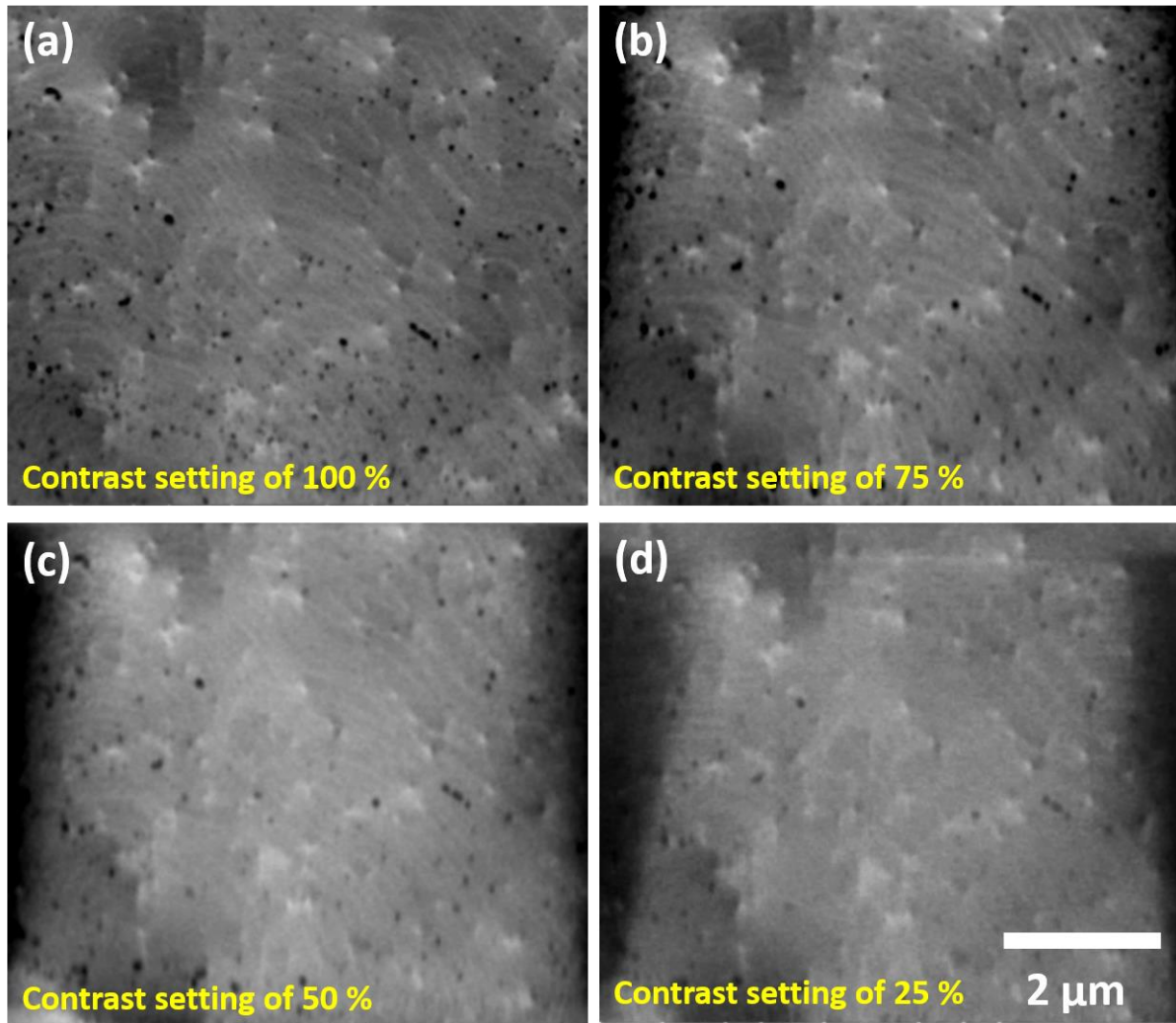


Fig. S1. The detector bias is varied by changing the contrast setting of the gaseous secondary electron detector to (a) 100 %, (b) 75%, (c) 50 % and (d) 25 %. The signal strength decreases as the bias voltage is decreased. All four ECCI micrographs are acquired with a same beam current and an acceleration voltage of 30 keV, dwell time of 100 $\mu$ s and a sample tilt of 64°.

### **S2 Effect of gas pressure**

Another factor affecting the gas amplification and the image resolution is the gas pressure. This is shown in Fig. S2 where the chamber pressure was increased from 0.3 mbar to 0.8 mbar. The images were acquired with the same beam current. At higher gas pressures images with improved signal to noise can be produced; however the resolution can be degraded. The black blotch in the middle of the image is a contaminant in the sample surface.

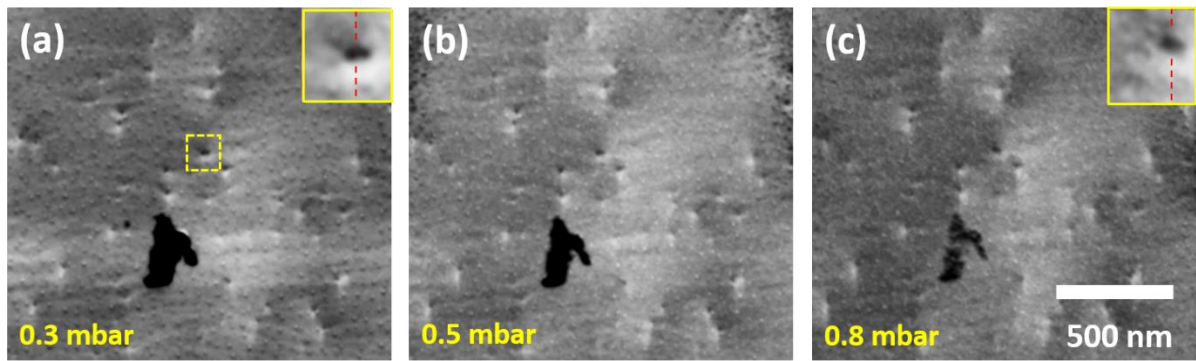


Fig. S2. Loss of spatial resolution as a function of gas pressure (a) 0.3 mbar, (b) 0.5 mbar and (c) 0.8 mbar. The inset image in (a) shows two dislocations can be resolved at a gas pressure of 0.3 mbar. However on increasing the gas pressure to 0.8 mbar (inset in image c), the individual dislocations are no longer resolved. All three ECCI micrographs are acquired with a same beam current and an acceleration voltage of 30 keV, dwell time of 100 $\mu$ s and a sample tilt of 52 $^{\circ}$ .

### S3 Effect of working distance

Since the path length for gas amplification has an effect on the current produced at the detector, the distance between the sample and the detector is also crucial to obtain good quality images. This can be investigated by changing the working distance (WD) as shown in Fig. S3 (the sample is moved since the detector is fixed). Ideally the longer the gas path length the greater the amplification, but moving too far away from the objective lens can also affect the image quality, particularly in low vacuum mode. However, a slight increase or decrease of the working distance does not appreciably affect the image quality as demonstrated in Fig. S3.

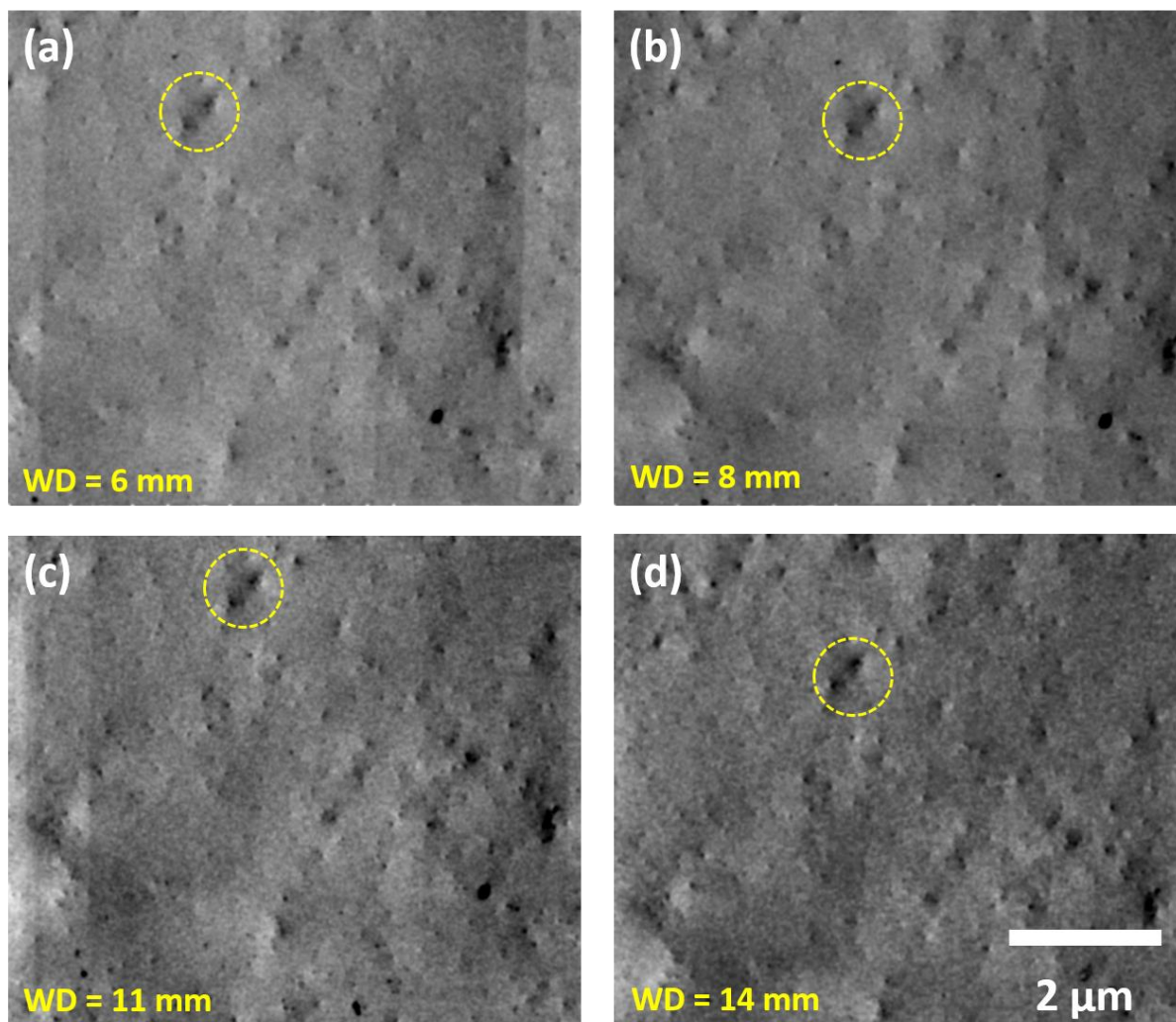


Fig. S3. Effect of gas amplification path length monitored by moving the sample away from the pole piece, thereby changing the working distance (WD) to (a) 6 mm, (b) 8 mm, (c) 11 mm and (d) 14 mm. The ECCI micrographs are acquired with a same beam current and an acceleration voltage of 30 keV, dwell time of 100 $\mu$ s and a sample tilt of 0 $^{\circ}$ .

#### **S4 Effect of scan rate**

Figure S4 shows the effect of beam dwell time ranging from 1  $\mu$ s to 1000  $\mu$ s. As expected, larger signal to noise images are produced for the longer scan duration. However, it is worth noting the dark and bright lines observed especially during longer scan duration (see Figures

S4c and S4d). We believe this is due to the fluctuation of gas pressure while acquiring the image and can remove it using FFT band-pass filtering.

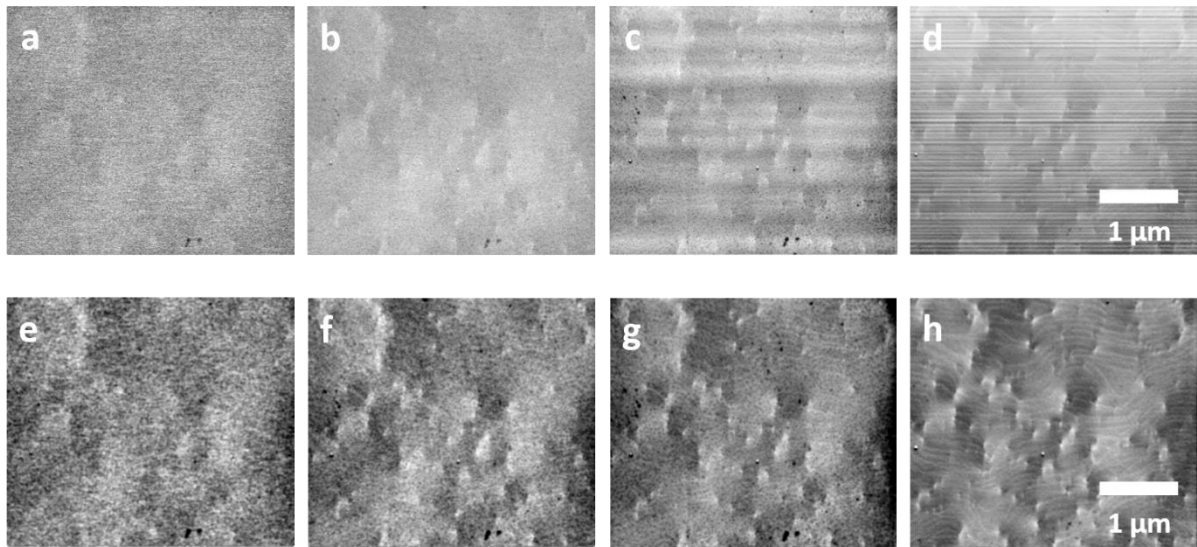


Fig. S4. ECCI micrographs taken with an image resolution of 1024 x 884 with dwell times of (a) 1  $\mu$ s, (b) 10  $\mu$ s, (c) 100  $\mu$ s and (d) 1000  $\mu$ s. The dark and bright horizontal lines observed when the scan time is long (c and d) are due to fluctuations in the gas pressure. (e-f) show the images after FFT band-pass filtering to remove the horizontal lines. The ECCI micrographs are acquired with a same beam current and an acceleration voltage of 30 keV and a sample tilt 52°.

### **S5 Effect of sample geometry**

Since the position of the GSEDs with respect to the sample is not crucial, ECCI can be performed in various scattering geometries. This is demonstrated in Fig. S5, which shows ECCI micrographs acquired in the backscatter geometry (Fig. S5a) and foreshatter geometry (Fig. S5b). There is a one to one correlation between the dislocations seen in both the images. However, tilting the sample changes the electron yield, which can modify the image contrast and the spatial resolution.

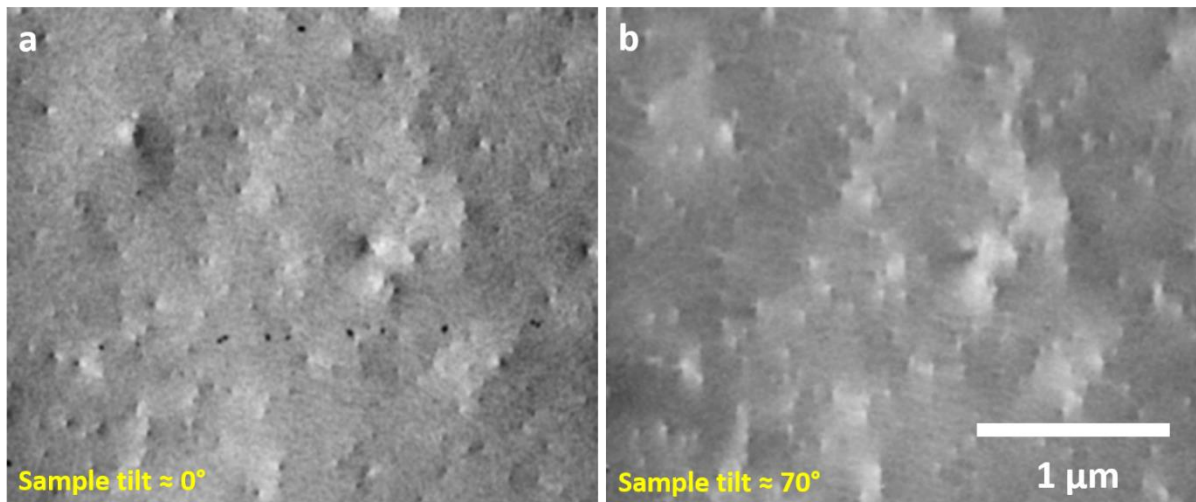


Fig. S5. The effect of sample geometry is shown here where one can see a one to one correlation between surface penetrating defects (threading dislocations) observed when the sample is at (a)  $0^\circ$  tilt, ideally used in the backscatter geometry and (b)  $70^\circ$  tilt, often used in the foreshatter geometry. The ECCI micrographs are acquired with a same beam current and an acceleration voltage of 30 keV and a dwell time of  $100\mu\text{s}$ .

### **S6 ECCI from larger samples (2 inch GaN semiconductor wafer)**

The non-destructive nature of the ECCI method becomes jeopardised when the original specimen needs to be modified or prepared (e.g. sectioned into small pieces) for structural analysis, as will often be necessary when the sample needs to be mounted at a high angle. Figure S6 shows an ECCI micrograph acquired using the large field detector from an intact as-grown 2 inch p-type GaN wafer. The image shown in Fig. S6a is a high magnification ECCI micrograph acquired from the centre of the wafer clearly revealing individual threading dislocations. The large area ECCI micrograph (lower magnification than Fig. S6a) shown in Fig. S6b is also from the centre of the wafer but revealing V- defects [2] (hexagonal features) commonly observed in III-nitride thin film structures. The threading dislocation density measured from the centre of the wafer is  $2.1 \pm 0.2 \times 10^8 \text{cm}^{-2}$ . In order to measure the

threading dislocation density from the corner of the wafer, we have moved the sample along the X-axis without tilting or rotating (i.e., not changing the channelling in condition). The acquired image is shown in Fig. S6c. Diffraction contrast can still be seen, revealing sub-grains and threading dislocations, which indicates that the sample does not have appreciable bowing. The threading dislocation density measured from the corner of the wafer is  $2.2 \pm 0.2 \times 10^8 \text{cm}^{-2}$ . There is no appreciable change in threading dislocation density, demonstrating the uniform quality of the sample.

Although the position of the gaseous secondary electron detectors is not crucial for performing ECCI, it is logical to use the backscatter geometry for characterising large samples as demonstrated in the present work. While conventional solid state BSE detectors can be used to image large samples, the use of an off-axis gaseous secondary electron detector can avoid unexpected accidents while tilting the sample towards the pole piece mounted solid state BSE detectors. Due to the limitations of our SEM chamber dimensions, we could only analyse a 2 inch wafer, however we could move anywhere on the sample and multiple images could be acquired and could be stitched together using commercial image stitching software [3]. The only limitation to characterising a large specimen (6, 8 or 12 inch wafers) is the size and geometry of the chamber.

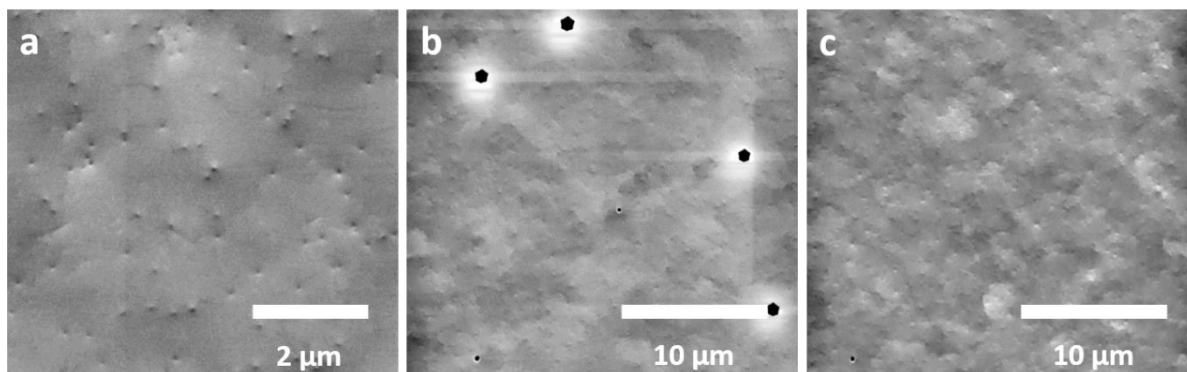


Fig. S6. ECCI micrographs of an Mg doped GaN acquired at  $18^\circ$  sample tilt with a same beam current and an acceleration voltage of 30 keV and a dwell time of  $100\mu\text{s}$ . (a) High magnification image revealing dislocations from the centre of the wafer, (b) large area and low magnification image taken from the centre of the wafer revealing V-defects in addition to threading dislocations and sub-grain boundaries and (c) image taken from the left corner of the wafer. The average threading dislocation density at the centre and the corner of the wafer is similar.

#### Supplementary references:

1. S. W. Morgan and M. R. Phillips *Journal of Microscopy*, **221** (2006) 183.
2. Y. Chen, T. Takeuchi, H. Amano, I. Akasaki, N. Yamada, Y. Kaneko, and S. Y. Wang, *Appl. Phys. Lett.* **72** (1998) 710. and/or I.-H. Kim, H.-S. Park, Y.-J. Park, and T. Kim, *Appl. Phys. Lett.* **73** (1998) 1634.
3. J. Chalfoun, M. Majurski, T. Blattner, K. Bhadriraju, W. Keyrouz, P. Bajcsy and M. Brady *Scientific Reports* **7** (2017) 4988.